Structural and Optical Properties of $Bi_{12}NiO_{19}$ Sillenite Crystals: Application for the Removal of Basic Blue 41 from Wastewater

Billal Brahimi [1], Hamza Kenfoud [2], Yasmine Benrighi [2] and Oussama Baaloudj [2],*

[1] Laboratory of Transfer Phenomena, Faculty of Mechanical Engineering and Process Engineering, University of Science and Technology Houari Boumediene (USTHB), BP 32, 16111 Algiers, Algeria; billalbrahimigpi@gmail.com

[2] Laboratory of Reaction Engineering, Faculty of Mechanical Engineering and Process Engineering, University of Science and Technology Houari Boumediene (USTHB), BP 32, 16111 Algiers, Algeria; hamza.kenfoud.93@gmail.com (H.K.); benrighiyasmine@gmail.com (Y.B.)

* Correspondence: obaaloudj@gmail.com; Tel.: +213-661-899-266

Abstract: This article covers the structural and optical property analysis of the sillenite $Bi_{12}NiO_{19}$ (BNO) in order to characterize a new catalyst that could be used for environmental applications. BNO crystals were produced by the combustion method using Polyvinylpyrrolidone as a combustion reagent. Different approaches were used to characterize the resulting catalyst. Starting with X-ray diffraction (XRD), the structure was refined from XRD data using the Rietveld method and then the structural form of this sillenite was illustrated for the first time. This catalyst has a space group of I23 with a lattice parameter of a = 10.24 Å. In addition, the special surface area (SSA) of BNO was determined by the Brunauer-Emmett-Teller (BET) method. It was found in the range between 14.56 and 20.56 $cm^2 \cdot g^{-1}$. Then, the morphology of the nanoparticles was visualized by Scanning Electron Microscope (SEM). For the optical properties of BNO, UV-VIS diffusion reflectance spectroscopy (DRS) was used, and a 2.1 eV optical bandgap was discovered. This sillenite's narrow bandgap makes it an effective catalyst for environmental applications. The photocatalytic performance of the synthesized $Bi_{12}NiO_{19}$ was examined for the degradation of Basic blue 41. The degradation efficiency of BB41 achieved 98% within just 180 min at pH ~9 and with a catalyst dose of 1 g/L under visible irradiation. The relevant reaction mechanism and pathways were also proposed in this work.

Keywords: sillenite $Bi_{12}NiO_{19}$; Rietveld method; optical properties; photodegradation; BB41 dye

1. Introduction

Traditional methods of water treatment cannot effectively eliminate pollutants from wastewaters and could cause great harm to the environment [1–4]. On the other hand, it has been shown that photocatalysis is a promising approach for the degradation of non-biodegradable compounds in water [5,6]. It is based on a photocatalyst that can be activated by light such as sunlight and using this energy to remove various types of pollutants [7]. Among these pollutants, basic blue 41 (BB41) has been identified as one of the most problematic dyes. It is present in industrial effluents and commonly used in acrylic, nylon, silk, cotton, and wool dyeing [8–10]. This dye is potentially fatal to living organisms. It is effective as a strainer for identifying avian leukocytes, blood, and bone marrow cells. It can also induce short periods of fast or difficult breathing when inhaled, and it can also cause nausea, vomiting, excessive perspiration, mental disorientation, and methemoglobinemia when consumed through the mouth [11]. Therefore, its detection and elimination are challenging goals. Based on our previous studies, photocatalysis-using catalysts have successfully removed both organic and inorganic pollutants in wastewater [12,13]. A novel catalyst with high photocatalytic activity and a narrow bandgap must be developed and tested in order to achieve this goal [14].

The increase in research in recent years for new material categories allowed new studies on structural and optical properties [15,16]. Among these materials—despite being relatively new—sillenites have attracted the attention of many researchers due to their unusual crystal formations, their peculiar electronics, their interesting photochromic, photorefractive, electro-optic, piezoelectric, dielectric properties, and promising optical activity [17–19]. They are used in various industrial applications, such as image amplification, phase conjugation, real-time and multiwavelength holography, optical memories for data storage, optical communications, signal processing and a variety of photocatalytic applications [20,21]. Sillenite crystals with a general formula of $Bi_{12}MO_{20x}$ (BMO) have a body-centered cubic crystal structure crystallized in the I23 space group [22]. Their overall structure is described by the atom of bismuth surrounded by seven oxygen atoms that share corners with other similar Bi polyhedrons and with MO_4 which represents a tetravalent ion or a combination of ions that exist both at the cube center and on the corners in the BMO structure [23,24]. There are a significant number of new sillenites that are used as photo-catalysts in previous research, such as $Bi_{12}TiO_{20}$ [25], $Bi_{12}GeO_{20}$ [21], $Bi_{12}PbO_{19}$ [22], $Bi_{12}CoO_{20}$ [26], $Bi_{12}SiO_{20}$ [21], $Bi_{12}MnO_{20}$ [17], $Bi_{12}FeO_{20}$ [27] and $Bi_{12}ZnO_{20}$ [28]. Among the sillenite crystals, bismuth nickelate $Bi_{12}NiO_{19}$ (BNO) has not been used as a photocatalyst yet, although it has recently gained considerable attention because of its tiny bandgap, its high photoconductivity, ease of separation of photogenerated electron-hole pairs and ease of recycling [29–31]. BNO is a single-phase multiferroic, which co-exists with ferroelasticity and has a magnetic character. It is also a lead-free and environmentally friendly material, which makes it very promising for photocatalytic applications. Due to its novelty in the photocatalyst field and its interesting proprieties, we selected BNO as a photocatalyst for this work.

We report in this study the synthesis of $Bi_{12}NiO_{19}$ sillenite by the sol-gel method using polyvinylpyrrolidone (PVP) as a combustion reagent. Firstly, the phase of the crystals was identified by X-ray diffraction (XRD); then, the structure and lattice constants of the phase were refined using the Rietveld method. The special surface area (SSA) of BNO was determined by the Brunauer–Emmett–Teller (BET) method. Then, the morphology of the nanoparticles was investigated by Scanning Electron Microscope (SEM). After that, the BNO's optical properties were investigated using UV-VIS diffusion reflectance spectroscopy (DRS), and the obtained bandgap was discussed. The photocatalytic activity of the sillenite $Bi_{12}NiO_{19}$ was tested for photodegradation of basic blue 41 dye.

2. Materials and Methods

2.1. Chemicals

Chemicals used in the present study were: nickel nitrate hexahydrate [$Ni(NO_3)_2 \cdot 6H_2O$] (98% Biochem), bismuth nitrate pentahydrate [$Bi(NO_3)_3 \cdot 5H_2O$] (98.5% Chem-Lab), Polyvinylpyrrolidone PVP K30 (Pharmalliance pharmaceutical company, Ouled Fayet, Algeria), ethanol (Biochem), nitric acid, HCl and NaOH (Sigma Aldrich; St. Louis, MO, USA). The basic blue 41 (>98% purity) was provided by Aldrich. Distilled water was used as a solvent. Without further purification, all chemicals were used as obtained.

2.2. Synthesis of the Sillenite $Bi_{12}NiO_{19}$

The $Bi_{12}NiO_{19}$ material (sillenite type) was synthesized by mixing nitrates of bismuth pentahydrate [$Bi(NO_3)_3 \cdot 5H_2O$], and nickel nitrate hexahydrate [$Ni(NO_3)_2 \cdot 6H_2O$] was dissolved in water using stoichiometric amounts (12:1 ratio). In order to improve the solubility of the solutions, nitric acid was added. The reaction was carried out according to the following equation:

$$12\ [Bi(NO_3)_3 \cdot 5H_2O] + [Ni(NO_3)_2 \cdot 6H_2O] \rightarrow Bi_{12}NiO_{19} + 38\ NO_2 + 66\ H_2O + 19/2\ O_2 \qquad (1)$$

After total solubilization, PVP K30 as a complexing agent was added to the reaction solution with a concentration of 15% *w/w* to obtain its complexing role [32]. The obtained solution was dehydrated by evaporation on a hot plate until it turned to a gel, then burned to form Xerogel, an amorphous powder, and after that denitrified at 600 °C for 3 h. Before

calcination, the obtained powder was homogenized by grinding in an agate mortar; it was calcined then in an air oven for 6 h at 800 °C. The calcination step was done to increase the crystallinity and to remove all carbonated waste left after the combustion reaction. All the synthesis process was summarized and illustrated in Figure 1. Then, the sample was subjected to phase identification, structural characterization and optical study.
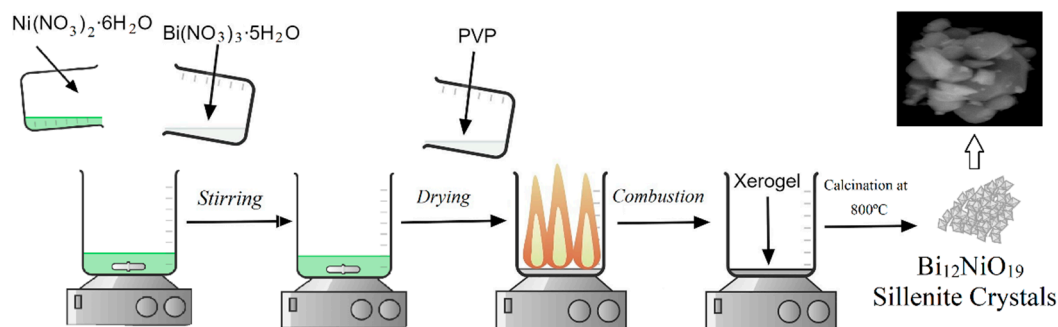

Figure 1. Process for preparing $Bi_{12}NiO_{19}$.

2.3. Characterization

X-ray diffraction (XRD) was conducted using a Phillips PW 1730. With the MAUD software (version 2.9.3), the Rietveld technique was used to measure structural properties, refinement and crystallinity. VESTA (version 3.4.0) was used to create the structure illustration. With an electron scanning microscope FEI Quanta 650, crystal pictures were captured. The sample's UV-visible diffuse reflection (DRS) was measured using a Cary 5000 UV-Vis spectrophotometer.

2.4. Photocatalysis Test

The photocatalytic degradation of Basic Blue 41 was carried out in a double-walled reactor with a magnetic stirring and cooling system. A 1 g/L dose of catalyst was suspended in a solution of BB41 aqueous solution with a concentration of 15 mg/L and pH ~9, which was found to be optimal conditions. The pH was modified by adding small amounts of HCl and NaOH. The adsorption experiment was performed in the absence of irradiation for 120 min before the photocatalysis test to reach the adsorption equilibrium. After the adsorption equilibrium, the reactor was exposed to visible irradiation using a tungsten lamp supplied by Osram (200 W). The temperature of the solution was maintained at a nearly constant 25 °C during the photocatalytic experiments using a thermostatic bath and a double-walled reactor as a cooling system. The concentration of BB41 was followed by measuring the absorbance in the wavelength (610 nm) with a UV–Vis spectrophotometer (OPTIZEN, UV-3220UV). The degradation efficiency was calculated from the relation:

$$\text{Degradation efficiency } \% = \frac{abs_{ad} - abs}{abs_{ad}} \times 100 \qquad (2)$$

where abs_{ad} and abs are the initial absorbance of BB41 and absorbance after time t, respectively.

3. Results

3.1. Characterization of the Sillenite $Bi_{12}NiO_{19}$

3.1.1. Phase Identification and Structural Investigation

To explore the formation of sillenite crystals $Bi_{12}NiO_{19}$, X-ray diffraction (XRD) was used (Figure 2). All diffraction peaks are attributed to the sillenite phase of $Bi_{12}NiO_{19}$ (JCPDS card, PDF No. 43-0448) [33]. This indicates good crystallization at 800 °C. The XRD data and I23 cubic structure were used to conduct Rietveld refinement, experimental findings and theoretical data determined by Maud are shown in Figure 2 as points and

red lines, respectively. According to the results, the findings estimated using the Rietveld technique matched well with the experimental X-ray diffraction pattern. The Rietveld refinement results gave identical results compared to other known methods of structural properties. [34,35]. Figure 1 also showed the purity and good crystallinity of our sillenite phase through the great congruence between the results of the experiment and the theoretical data. It was determined that the refined values represented a cubic form with a space group of I23 and a lattice parameter of a = 10.24 Å. The Rietveld refined parameters such as reliability factors R_p, R_{exp}, R_{wp} and Sig with the cell parameter (a) and atomic position (x,y,z) are presented in Table 1.
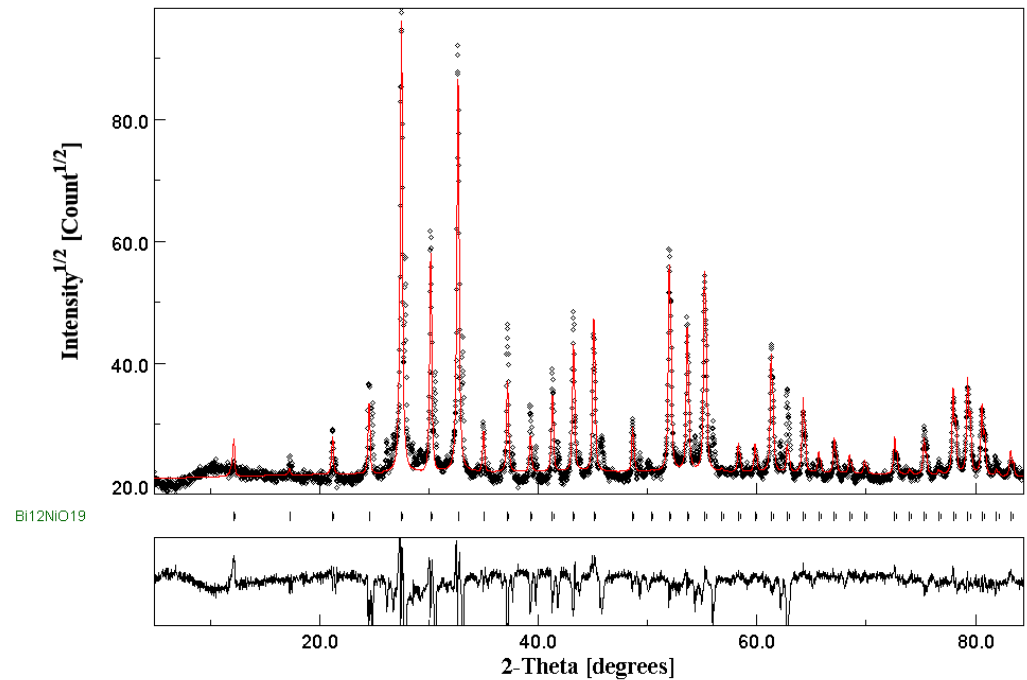

Figure 2. XRD diffractogram of $Bi_{12}NiO_{19}$ with Reitveld refinement.

Table 1. Structural and lattice parameters.

Phase		$Bi_{12}NiO_{19}$			
Groupe Space		I 2 3			
a (Å)		10.244759			
	Atom	x	y	z	Biso
	Ni1	0.000000	0.000000	0.000000	0.077
	Ni2	0.8216535	0.68130636	0.9814812	0.077
Atoms	Bi1	0.000000	0.000000	0.000000	0.923
	Bi2	0.9814812	0.68130636	0.8216535	0.923
	O1	0.83216524	0.6798176	0.459461	1
	O2	0.729963	0.729963	0.729963	1
	O3	0.123646714	0.123646714	0.123646714	0.75
V (Å³)		1083.4283			
D (nm)		59.46			
	Rb	9.5436			
R Factors	Rexp	4.0007			
	Rwp	14.3421			
	Sig	3.58			

The structural representation of the sillenite BNO was illustrated in Figure 3 by Vesta using the structural parameters in Table 1. The atoms' colors for Ni, Bi and O are green, yellow and red, respectively. As can be seen, the phase is a cubic structure (space group I23). The atoms in the crystal structure show shared occupancy between bismuth and nickel while bismuth atoms are dominant at around 92% due to the ratio of atoms being 12:1 for bismuth and nickel.
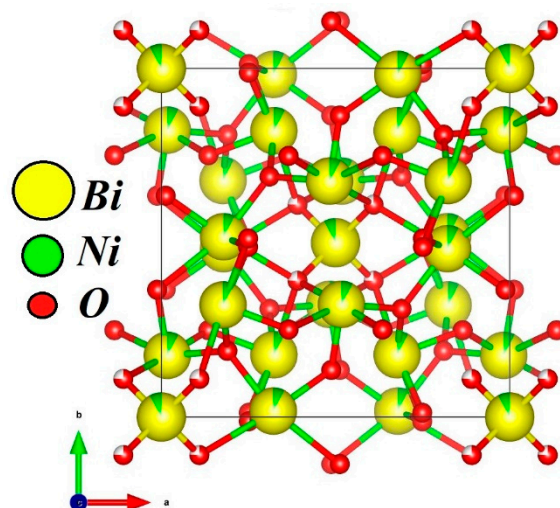

Figure 3. The structural representation of the crystal $Bi_{12}NiO_{19}$.

The crystallite size, X-ray density, and special surface area were calculated from the following equations [36]:

$$D = \frac{K\lambda}{\beta \cos(\theta)} \quad (3)$$

$$\rho = \frac{ZM}{N_A V} \quad (4)$$

$$S = \frac{6 \times 10^3}{D \times \rho} \quad (5)$$

where D is the regular phase crystallite, K is the Scherener constant, β is the full width at the highest half of the phase, θ is the angle Braggs, N_A is Avogadro's number, M is the Molecular mass of BNO (2870.45 g·mol^{-1}), ρ is the density of X-ray, Z is the count of model units in a cell ($Z = 2$ for sillenites [26]) and V is the unit cell volume (1083.428335 A 3) and S is the specific surface area.

The crystallite size was calculated from the main peaks of the XRD diffractogram, and it was found in the range between 33.20 and 33.20 nm. The density of X-rays was found to be 8.79 g·cm^{-3}. The special surface area (SSA) of the particular BNO was estimated by the Brunauer–Emmett–Teller (BET) method in Equation (4), and it was found in the range between 14.56 and 20.56 cm^2·g^{-1}.

3.1.2. Morphology Investigation

In order to analyze the morphology of the BNO crystals, a Scanning Electron Microscopy (SEM) was used. Figure 4 shows typical SEM images of the BNO crystals. A small agglomeration can be seen due to the ultrafine nature of the sample [37]. This leads to a non-uniform distribution of crystals of different shapes and a noticeable porosity in the sample [28]. The viscosity of the suspension in the synthesis route plays an important role in the development of the porous structure [1,38]. The viscosity of suspension during synthesis causes the porous structure to get compacted. The sol-gel method is well-known for its great viscosity because it forms a gel during the synthesis. Due to this, we have significant porosity in our sample.
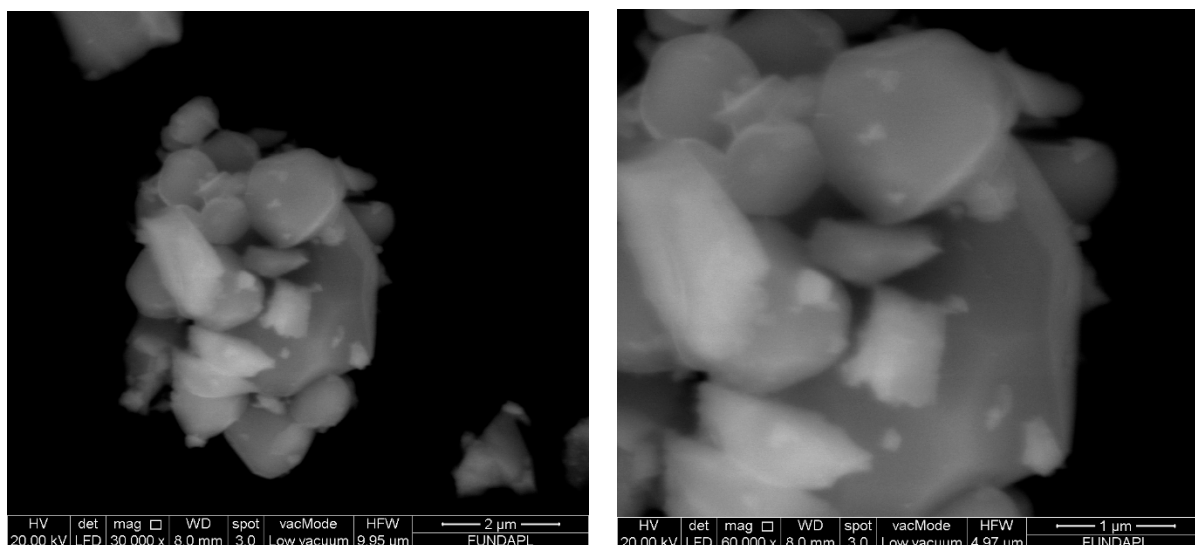
Figure 4. SEM images of the crystals $Bi_{12}NiO_{19}$.

3.1.3. Optical Study

To determine the catalyst's performance, knowledge about the gap is highly necessary. The optical properties of BNO crystals were investigated using UV-vis diffuse reflectance spectroscopy (DRS). The bandgap energy (E_g) is determined by plotting the Tauc plot (Figure 5), which is the dependence of the absorption coefficient (α) on the photon energy (hv). It is expressed in the following relationship [37,39]:

$$(\alpha hv)^{\frac{1}{n}} = K(hv - E_g) \tag{6}$$

where α is the absorption coefficient, K is a proportionality constant, and the exponent $n=$ 2 or 1/2 refers to the nature of the transition. The direct bandgap was estimated by the interception of the linear plot $(\alpha hv)^2$ and the hv axis. The band-gap energy (E_g) of NBO crystals was about 2.1 $\pm$ 0.1 eV which is a smaller bandgap than of TiO_2 and ZnO (3.2 eV) [40,41]. This shows that BNO has a significant absorption level for both UV and visible light from wavelength 200 to 800 nm where the fraction of the light irradiance is converted into electrical and/or chemical energy. This tends to be more effective than the photocatalysts ZnO and TiO_2 and leads in visible light irradiation to an increase in the formation of pairs of electron holes. This sillenite's narrow bandgap makes it a new promising catalyst for photocatalysis applications for environmental aquatic pollution.
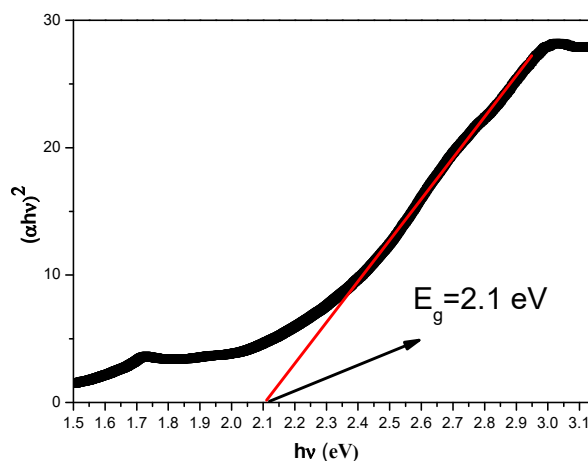

Figure 5. UV–Vis diffuse reflectance spectrum of the crystals $Bi_{12}NiO_{19}$.

3.2. Photocatalytic Activity

To test the photocatalytic activity of this catalyst, BB41 was selected as a topical example of organic pollutants. The photolysis effect of irradiation must be taken into account. An irradiation test for the elimination of the effects of photolysis was carried without the Catalyst BNO. Photolysis showed only a small percentage of BB41 degradation, not even above 5% percent. The effects of photolysis could consequently be overlooked. After that, the test was performed in the presence of the catalyst BNO. Before illumination of the photocatalytic reactor, it is important to eliminate the adsorption effect in a dark condition, the adsorption has not a significant removal for BB41.

After that, photocatalysis tests were started by the effect of pH, as the pH played a major role in the degradation. The tests were done in different pH mediums with a concentration of 15 mg/L and a catalyst dose of 1 g/L for 3 h, the results are shown in Figure 6. As can be seen, pH 9 was the optimal pH condition, because BB41 is a cationic dye, its photodegradation is favored in the basic medium, and the photodegradation performance of BNO for BB41 is boosted in the basic condition.
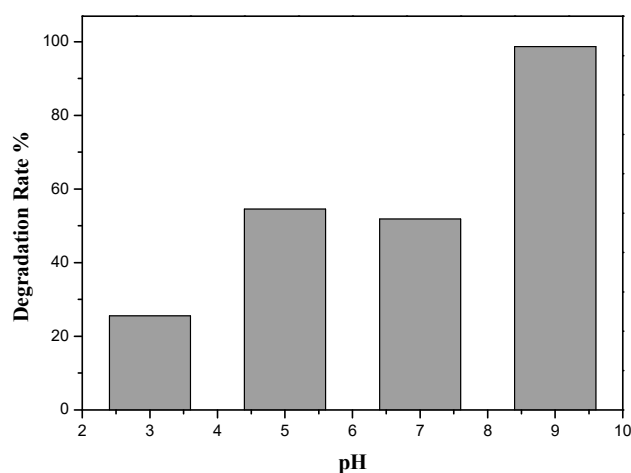

Figure 6. Effect of pH on the degradation of BB41.

After selecting the optimal pH, a test with a kinetic study was carried out under optimal conditions. The results are illustrated in Figure 7; Figure 7a shows the evolution of BB41 degradation as a function of time, where Figure 7b shows the associated UV-vis spectra for each point and the absorption peaks of BB41 at 610 nm can be observed decreasing with time. As can be observed, the degradation efficiency of BB41 achieved 98% within just 180 min at pH ~9 and 25 °C. This result can be explained by the gap energy of the catalyst (2.1 eV), which offers a higher absorption in both UV and visible areas from 200 to 800 mm [42].

It was already demonstrated in our previous works [13,14] that the degradation of the dye as an organic compound in the photocatalytic process is mainly due to the reactive oxidative species (ROS) such as superoxide radicals ($O_2^{\bullet-}$) and hydroxyl radicals ($^{\bullet}OH$), where the electrons of $Bi_{12}NiO_{19}$ conduction band are degraded the Basic Blue 41 by reducing the absorbed O_2 to the super-radical anion $O_2^{\bullet-}$. The oxidation occurs concomitantly by radicals $^{\bullet}OH$ through a valence band that reacts with H_2O [43]. In order to investigate the active species for the degradation of BB41, isopropanol and benzoquinone were chosen as scavenger agents to capture $^{\bullet}OH$ and $O_2^{\bullet-}$, respectively. Figure 8 shows the degradation efficiency with and without the presence of scavengers.
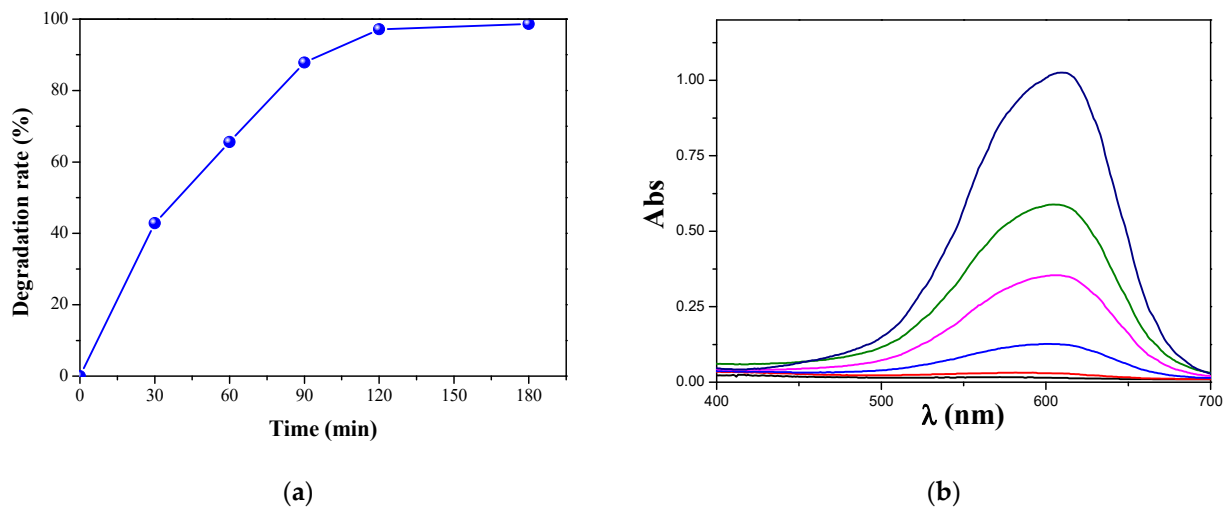
Figure 7. (**a**) Photocatalytic efficiency on BB 41 as a function of time [C_o = 15 mg/L, dose =1 g/L, pH ~ 9 and T = 25 °C]. (**b**) UV–visible spectra.
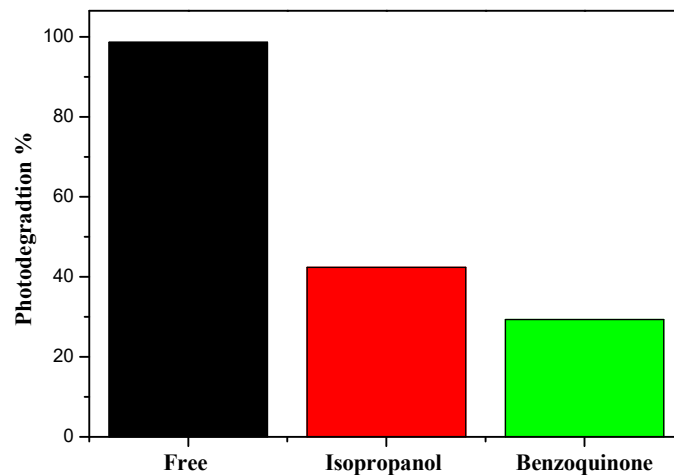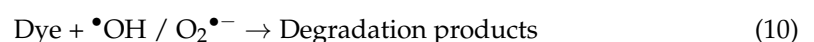

Figure 8. Effect of scavengers on the degradation of BB41.

As can be seen, adding benzoquinone and isopropanol to the solution reduced the BB41 degradation efficiency, indicating that both $O_2^{\bullet-}$ and $^{\bullet}OH$ were important active species in the photocatalytic activity. The photocatalytic reactions that occur at the solid/liquid interface can be bonded according to the following reaction mechanism:

$$Bi_{12}NiO_{19} + hv \rightarrow e^-_{\ CB} + h^+_{\ VB} \tag{7}$$

$$h^+_{\ VB} + H_2O \rightarrow {}^{\bullet}OH + H^+ \tag{8}$$

$$e^-_{\ CB} + O_2 \rightarrow O_2^{\bullet-} \tag{9}$$

$$Dye + {}^{\bullet}OH\ /\ O_2^{\bullet-} \rightarrow Degradation\ products \tag{10}$$

4. Conclusions

The main objective of this work was devoted to the study of the structural and optical properties of $Bi_{12}NiO_{19}$ and its application as a photocatalyst for the disposal of the basic blue 41 dye, used in the textile industry, under visible irradiation. BNO nanoparticles were synthesized using the combustion method using Polyvinylpyrrolidone as a combustion reagent. Different approaches were used to characterize the resulting catalyst. Starting with X-ray diffraction (XRD), the Rietveld method was used to refine the structure based on XRD data. which showed the purity and good crystallinity of our sillenite phase. Then,

the structural form of this sillenite was illustrated for the first time. This catalyst has a space group of I23 with a lattice parameter of (a = 10.24 Å) for this catalyst. The special surface area (SSA) of BNO was determined by the Brunauer–Emmett–Teller (BET) method, it was found in the range between 14.56 and 20.56 $cm^2 \cdot g^{-1}$. Then, the morphology of the nanoparticles was visualized by Scanning Electron Microscope (SEM). Finally, the optical properties of BNO were determined by UV-VIS diffusion reflectance spectroscopy (DRS), a 2.1 eV optical bandgap was discovered. This narrow bandgap and the good crystallinity allow this sillenite to be a promising and effective catalyst for photocatalytic applications in the environmental field such as the treatment of polluted water under visible light radiation. That was confirmed by the application of this sillenite by performing the decomposition of the basic blue 41 dye under visible irradiation where a total degradation was obtained at pH ~9 and 25 °C in less than 180 min. For future research, we will test the effects of this sillenite on the degradation and reduction of organic and inorganic pollutants, as they are both hazardous contaminants to the environment.

Author Contributions: Conceptualization, O.B. and H.K.; methodology, O.B. and Y.B.; software, O.B.; validation, O.B. and B.B.; formal analysis, B.B.; investigation, Y.B. and O.B.; resources, B.B.; data curation, O.B.; writing—original draft preparation, O.B., H.K., B.B. and Y.B.; writing—review and editing, O.B.; visualization, O.B.; supervision, O.B.; All authors have read and agreed to the published version of the manuscript.

Institutional Review Board Statement: Not applicable.

Informed Consent Statement: Not applicable.

Data Availability Statement: Not applicable.

Conflicts of Interest: The authors declare that they have no conflict of interest.

References

1. Baaloudj, O.; Nasrallah, N.; Kebir, M.; Khezami, L.; Amrane, A.; Assadi, A.A. A comparative study of ceramic nanoparticles synthesized for antibiotic removal: Catalysis characterization and photocatalytic performance modeling. *Environ. Sci. Pollut. Res.* **2020**, *28*, 13900–13912. [CrossRef] [PubMed]
2. Achour, S.; Amokrane, S.; Chegrouche, S.; Nibou, D.; Baaloudj, O. Artificial neural network modeling of the hexavalent uranium sorption onto chemically activated bentonite. *Res. Chem. Intermed.* **2021**, *24*, 1–8. [CrossRef]
3. Asadi-Ghalhari, M.; Mostafaloo, R.; Ghafouri, N.; Kishipour, A.; Usei, S.; Baaloudj, O. Removal of Cefixime from aqueous solutions via proxy electrocoagulation: Modeling and optimization by response surface methodology. *React. Kinet. Mech. Catal.* **2021**, *27*, 1–13. [CrossRef]
4. Bourkeb, K.; Baaloudj, O. Facile electrodeposition of ZnO on graphitic substrate for photocatalytic application: Degradation of antibiotic in a continuous stirred-tank reactor. *J. Solid State Electrochem.* **2021**, *6*, 1–8. [CrossRef]
5. Benrighi, Y.; Nasrallah, N.; Chaabane, T.; Sivasankar, V.; Darchen, A.; Baaloudj, O. Photocatalytic performances of $ZnCr_2O_4$ nanoparticles for cephalosporins removal: Structural, optical and electrochemical properties. *Opt. Mater.* **2021**, *115*, 111035. [CrossRef]
6. Brahimi, B.; Mekatel, E.; Mellal, M.; Trari, M. Synthesis of the hexaferrite semiconductor $SrFe_{12}O_{19}$ and its application in the photodegradation of Basic Red 46. *J. Mater. Sci. Mater. Electron.* **2021**, *32*, 11780–11790. [CrossRef]
7. Thi Mai Tho, N.; The Huy, B.; Nha Khanh, D.N.; Quoc Thang, N.; Thi Phuong Dieu, N.; Dai Duong, B.; Thi Kim Phuong, N. Mechanism of Visible-Light Photocatalytic Mineralization of Indigo Carmine Using $ZnBi_2O_4$-Bi_2S_3 Composites. *ChemistrySelect* **2018**, *3*, 9986–9994. [CrossRef]
8. Mahmoodi, N.M. Magnetic ferrite nanoparticle-alginate composite: Synthesis, characterization and binary system dye removal. *J. Taiwan Inst. Chem. Eng.* **2013**, *44*, 322–330. [CrossRef]
9. Mahmoodi, N.M. Surface modification of magnetic nanoparticle and dye removal from ternary systems. *J. Ind. Eng. Chem.* **2015**, *162*, 251–259. [CrossRef]
10. Mahmoodi, N.M.; Abdi, J.; Oveisi, M.; Alinia Asli, M.; Vossoughi, M. Metal-organic framework (MIL-100 (Fe)): Synthesis, detailed photocatalytic dye degradation ability in colored textile wastewater and recycling. *Mater. Res. Bull.* **2018**, *100*, 357–366. [CrossRef]
11. Mahmoodi, N.M.; Keshavarzi, S.; Ghezelbash, M. Synthesis of nanoparticle and modelling of its photocatalytic dye degradation ability from colored wastewater. *J. Environ. Chem. Eng.* **2017**, *5*, 3684–3689. [CrossRef]

12. Kenfoud, H.; Nasrallah, N.; Baaloudj, O.; Meziani, D.; Chaabane, T.; Trari, M. Photocatalytic reduction of Cr(VI) onto the spinel $CaFe_2O_4$ nanoparticles. *Optik* **2020**, *223*, 165610. [CrossRef]

13. Baaloudj, O.; Nasrallah, N.; Kebir, M.; Guedioura, B.; Amrane, A.; Nguyen-Tri, P.; Nanda, S.; Assadi, A.A. Artificial neural network modeling of cefixime photodegradation by synthesized $CoBi_2O_4$ nanoparticles. *Environ. Sci. Pollut. Res.* **2020**, *28*, 15436–15452. [CrossRef] [PubMed]

14. Baaloudj, O.; Assadi, I.; Nasrallah, N.; El, A.; Khezami, L. Simultaneous removal of antibiotics and inactivation of antibiotic-resistant bacteria by photocatalysis: A review. *J. Water Process Eng.* **2021**, *42*, 102089. [CrossRef]

15. Oliveira, O.G.; Mincache, A.J.; Dias, G.S.; Santos, I.A.; Guo, R.; Bhalla, A.S.; Cótica, L.F. Study of the crystal and electronic structures of $(Bi1-xNdx)FeO_3$ compositions using Rietveld refinements and the maximum entropy method. *Ferroelectrics* **2019**, *545*, 167–174. [CrossRef]

16. Im, W.B.; Page, K.; Denbaars, S.P.; Seshadri, R. Probing local structure in the yellow phosphor $LaSr_2 AlO_5:Ce^{3+}$, by the maximum entropy method and pair distribution function analysis. *J. Mater. Chem.* **2009**, *19*, 8761–8766. [CrossRef]

17. Wu, X.; Li, M.; Li, J.; Zhang, G.; Yin, S. A sillenite-type $Bi_{12}MnO_{20}$ photocatalyst: UV, visible and infrared lights responsive photocatalytic properties induced by the hybridization of Mn 3d and O 2p orbitals. *Appl. Catal. B Environ.* **2017**, *219*, 132–141. [CrossRef]

18. Lin, X.; Huang, F.; Wang, W.; Xia, Y.; Wang, Y.; Liu, M.; Shi, J. Photocatalytic activity of a sillenite-type material $Bi_{25}GaO_{39}$. *Catal. Commun.* **2008**, *9*, 572–576. [CrossRef]

19. Zhang, H.; Lü, M.; Liu, S.; Xiu, Z.; Zhou, G.; Zhou, Y.; Qiu, Z.; Zhang, A.; Ma, Q. Preparation and photocatalytic properties of sillenite $Bi_{12}TiO_{20}$ films. *Surf. Coat. Technol.* **2008**, *202*, 4930–4934. [CrossRef]

20. Lima, A.F.; Lalic, M.V. First-principles study of the $BiMO_4$ antisite defect in the $Bi_{12}MO_{20}$ (M = Si, Ge, Ti) sillenite compounds. *J. Phys. Condens. Matter.* **2013**, *25*, 495505. [CrossRef]

21. Hou, D.; Hu, X.; Wen, Y.; Shan, B.; Hu, P.; Xiong, X.; Qiao, Y.; Huang, Y. Electrospun sillenite $Bi_{12}MO_{20}$ (M = Ti, Ge, Si) nanofibers: General synthesis, band structure, and photocatalytic activity. *Phys. Chem. Chem. Phys.* **2013**, *15*, 20698–20705. [CrossRef]

22. Yao, W.F.; Wang, H.; Xu, X.H.; Zhou, J.T.; Yang, X.N.; Zhang, Y.; Shang, S.X.; Wang, M. Sillenites materials as novel photocatalysts for methyl orange decomposition. *Chem. Phys. Lett.* **2003**, *377*, 501–506. [CrossRef]

23. Yao, W.F.; Xu, X.H.; Zhou, J.T.; Yang, X.N.; Zhang, Y.; Shang, S.X.; Wang, H.; Huang, B.B. Photocatalytic property of sillenite $Bi_{24}AlO_{39}$ crystals. *J. Mol. Catal. A Chem.* **2004**, *212*, 323–328. [CrossRef]

24. Valant, M.; Suvorov, D. Processing and Dielectric Properties of Sillenite Compounds $Bi_{12}MO_{20}$-δ (M: Si, Ge, Ti, Pb, Mn, $B_{1/2}P_{1/2}$). *ChemInform* **2010**, *33*, 2900–2904. [CrossRef]

25. Noh, T.H.; Hwang, S.W.; Kim, J.U.; Yu, H.K.; Seo, H.; Ahn, B.; Kim, D.W.; Cho, I.S. Optical properties and visible light-induced photocatalytic activity of bismuth sillenites ($Bi_{12}XO_{20}$, X = Si, Ge, Ti). *Ceram. Int.* **2017**, *43*, 12102–12108. [CrossRef]

26. Kenfoud, H.; Baaloudj, O.; Nasrallah, N.; Bagtache, R.; Assadi, A.A.; Trari, M. Structural and electrochemical characterizations of $Bi_{12}CoO_{20}$ sillenite crystals: Degradation and reduction of organic and inorganic pollutants. *J. Mater. Sci. Mater. Electron.* **2021**, *32*, 16411–16420. [CrossRef]

27. Vavilapalli, D.S.; Melvin, A.A.; Bellarmine, F.; Mannam, R.; Velaga, S.; Poswal, H.K.; Dixit, A.; Ramachandra Rao, M.S.; Singh, S. Growth of sillenite Bi^+FeO^+ single crystals: Structural, thermal, optical, photocatalytic features and first principle calculations. *Sci. Rep.* **2020**, *10*, 22052. [CrossRef] [PubMed]

28. Baaloudj, O.; Nasrallah, N.; Assadi, A.A. Facile synthesis, structural and optical characterizations of $Bi_{12}ZnO_{20}$ sillenite crystals: Application for Cefuroxime removal from wastewater. *Mater. Lett.* **2021**, *304*, 130658. [CrossRef]

29. Zhoua, P.; Xiaoa, F.; Jia, L. $Bi_{12}NiO_{19}$ micro-sheets grown on graphene oxide: Temperature-dependent facile synthesis and excellent electrochemical behavior for supercapacitor electrode. *J. Electroanal. Chem.* **2021**, *884*, 115075. [CrossRef]

30. Pei, L.Z.; Wei, T.; Lin, N.; Zhang, H. Synthesis of bismuth nickelate nanorods and electrochemical detection of tartaric acid using nanorods modified electrode. *J. Alloys Compd.* **2016**, *663*, 677–685. [CrossRef]

31. Rajamoorthy, M.; Geetha, D.; Sathiya Priya, A. Synthesis of Cobalt-Doped $Bi_{12}NiO_{19}$: Structural, Morphological, Dielectric and Magnetic Properties. *Arab. J. Sci. Eng.* **2021**, *46*, 737–744. [CrossRef]

32. Giannopoulou, I.; Saïs, F.; Thomopoulos, R. Handbook-of-pharmaceutical-excipients-6th-edition. *Rev. Nouv. Technol. Inf.* **2015**, *E28*, 257–262.

33. Ma, Y.; Qiu, F.L.; Wei, T.; Lin, F.F.; Yan, L.; Wu, H.; Zhang, Y.; Pei, L.Z.; Fan, C.G. Facile Synthesis of Polyaniline/Bismuth Nickelate Nanorod Composites for Sensitive Tartaric Acid Detection. *Surf. Eng. Appl. Electrochem.* **2019**, *55*, 335–341. [CrossRef]

34. Yé, Z.G.; Crottaz, O.; Vaudano, F.; Kubel, F.; Tissot, P.; Schmid, H. Single crystal growth, structure refinement, ferroelastic domains and phase transitions of the hausmannite $CuCr_2O_4$. *Ferroelectrics* **2011**, *162*, 103–118. [CrossRef]

35. Dollase, W.A.; O'Neill, H.S.C. The spinels $CuCr_2O_4$ and $CuRh_2O_4$. *Acta Crystallogr. Sect. C Cryst. Struct. Commun.* **1997**, *53*, 657–659. [CrossRef]

36. Karuppasamy, P.; Senthil Pandian, M.; Ramasamy, P.; Verma, S. Crystal growth, structural, optical, thermal, mechanical, laser damage threshold and electrical properties of triphenylphosphine oxide 4-nitrophenol (TP4N) single crystals for nonlinear optical applications. *Opt. Mater.* **2018**, *79*, 152–171. [CrossRef]

37. Kenfoud, H.; Nasrallah, N.; Baaloudj, O.; Derridj, F.; Trari, M. Enhanced photocatalytic reduction of Cr(VI) by the novel hetero-system $BaFe_2O_4/SnO_2$. *J. Phys. Chem. Solids* **2022**, *160*, 110315. [CrossRef]

38. Tripathy, S.; Saini, D.S.; Bhattacharya, D. Synthesis and fabrication of $MgAl_2O_4$ ceramic foam via a simple, low-cost and eco-friendly method. *J. Asian Ceram. Soc.* **2016**, *4*, 149–154. [CrossRef]

39. Makuła, P.; Pacia, M.; Macyk, W. How to Correctly Determine the Band Gap Energy of Modified Semiconductor Photocatalysts Based on UV-Vis Spectra. *J. Phys. Chem. Lett.* **2018**, *9*, 6814–6817. [CrossRef]

40. Serpone, N. Is the band gap of pristine TiO_2 narrowed by anion- and cation-doping of titanium dioxide in second-generation photocatalysts? *J. Phys. Chem. B* **2006**, *110*, 24287–24293. [CrossRef]

41. Miki-yoshida, M. Optical Band Gap Estimation of ZnO Nanorods a E = B^E − Eg h. *Mat. Res.* **2016**, *19*, 33–38. [CrossRef]

42. Baaloudj, O.; Assadi, A.A.; Azizi, M.; Kenfoud, H.; Trari, M.; Amrane, A.; Assadi, A.A.; Nasrallah, N. Synthesis and Characterization of $ZnBi_2O_4$ Nanoparticles: Photocatalytic Performance for Antibiotic Removal under Different Light Sources. *Appl. Sci.* **2021**, *11*, 3975. [CrossRef]

43. Kenfoud, H.; Nasrallah, N.; Meziani, D.; Trari, M. Photoelectrochemical study of the spinel $CaFe_2O_4$ nanostructure: Application to Basic Blue 41 oxidation under solar light. *J. Solid State Electrochem.* **2021**, *25*, 1815–1823. [CrossRef]